particles

MDPI

Review

Nuclear Exotic Structures, Exotic Decays and Near-Barrier Reactions

Cheng Yin, Chengjian Lin *, Lei Yang *, Feng Yang, Huiming Jia, Nanru Ma, Peiwei Wen and Tianpeng Luo

China Institute of Atomic Energy, P.O. Box 275(10), Beijing 102413, China
* Correspondence: cjlin@ciae.ac.cn (C.L.); yang_lei@ciae.ac.cn (L.Y.)

Abstract

The reaction dynamics of weakly-bound nuclear systems at near-barrier energies is a compelling topic in nuclear physics. This review summarizes decades of experimental work by the Nuclear Reaction Group at the China Institute of Atomic Energy. Using transfer reactions with the distorted wave born approximation and asymptotic normalization coefficient analyses, we confirm the first excited neutron halo (^{13}C) on the β-stability line and identified new halo states in ^{12}B. Total reaction cross-section measurements revealed proton halo nuclei ^{27}P and ^{29}S, with core enlargement observed in ^{27}P and ^{28}P. We established conditions for halo formation and delineated the proton halo existence region. In two-proton emission studies, we observed ^{2}He cluster emission from highly excited ^{17,18}Ne and ^{28,29}S, with ^{29}S being the second such case internationally. In β-delayed decay, we discovered β2p emission in ^{22}Si and determined its mass, observing isospin-symmetry breaking in ^{20}Mg, ^{22}Si, and ^{27}S. Decay schemes for ^{27}S and ^{26}P addressed the ^{26}Al abundance problem. For nuclear interactions, we investigated the ^{6}He optical potential, finding the dispersion relation inapplicable for ^{6}He + ^{209}Bi, and developed notch and Bayesian methods to constrain uncertainties. For unstable nuclei, the proton drip-line systems ^{8}B and ^{17}F have been intensively studied via complete kinematics measurements of the ^{8}B + ^{120}Sn and ^{17}F + ^{58}Ni reactions, respectively. The results show that elastic breakup dominates for proton-halo ^{8}B, while inelastic breakup prevails for ^{17}F, with proton-rich nuclei exhibiting lower breakup probabilities than neutron-halo nuclei due to Coulomb effects. Fusion studies revealed sub-barrier enhancement in ^{17}F + ^{58}Ni from continuum couplings. We propose direct fusion–evaporation measurements with deflection systems integrated with breakup detection to disentangle complete and incomplete fusion channels.

Keywords: exotic nuclei; exotic structures and decays; optical potential; near-barrier reaction dynamics

Check for updates

Academic Editor: Armen Sedrakian

Received: 27 February 2026
Revised: 31 March 2026
Accepted: 9 April 2026
Published: 1 May 2026

Copyright: © 2026 by the authors. Licensee MDPI, Basel, Switzerland. This article is an open access article distributed under the terms and conditions of the Creative Commons Attribution (CC BY) license.

1. Introduction

With the development of radioactive ion beam facilities and detection techniques, the scope of nuclear physics research has rapidly expanded towards nuclei far from the β-stability line. The study of reaction mechanisms induced by radioactive nuclear beams at energies around the Coulomb barrier has emerged as a hot topic in contemporary nuclear physics [1–4]. Compared to stable nuclei, these nuclei far from the stability line generally possess lower separation energies and are more loosely bound; hence, they are referred to as weakly bound nuclei. This characteristic endows them with exotic structures, such as halos, skins, and clusters. In 1985, Tanihata et al. measured interaction cross-sections of light unstable nuclei and, using a Glauber-type analysis to extract matter radii, first

identified the anomalously large radius of ^{11}Li, revealing an extended nuclear structure associated with weakly bound neutrons [5,6]. Subsequently, in 1987, Hansen and Jonson first proposed the concept of halo nuclei [7]. For tightly bound nuclear systems, only a few reaction channels, such as fusion, inelastic scattering, and transfer reactions, are typically open at energies around the Coulomb barrier. In contrast, the reaction mechanisms for weakly bound nuclear systems are considerably more complex. Due to their low breakup thresholds, the projectile can easily break up during the reaction. The emergence of the breakup channel can induce strong coupling effects on other channels like elastic scattering and fusion, thereby influencing the overall reaction dynamics of the system.

The Nuclear Reaction Group at the China Institute of Atomic Energy (CIAE) has conducted rigorous and comprehensive studies on the reaction dynamics of weakly bound nuclear systems at energies around the Coulomb barrier. Over the past two decades, the group has continuously dedicated substantial efforts to refining experimental techniques and optimizing data analysis methods. In elucidating the characteristics of the interaction potential and reaction mechanisms of weakly bound nuclear systems, a series of groundbreaking discoveries have been achieved. Given the significant progress and profound insights gained from these studies, there is an urgent need to conduct a comprehensive review and synthesis of the research findings. By integrating the outcomes and literature data from these studies, we can not only systematically summarize the scientific implications of the experimental observations but also provide important guidance for future research directions.

The structure of this review is as follows. We start from the exotic structures and decay modes of nuclei near the particle emission threshold in Section 1. Transfer reactions and the Distorted Wave Born Approximation (DWBA)/Asymptotic Normalization Coefficient (ANC) analyses are introduced to extract halo states and density distributions, with new neutron and proton halos identified. The existence conditions for halo formation and the proton halo region are delineated. Two-proton correlated emission and β-delayed decay studies of proton-rich nuclei are presented, including the discovery of β2p emission in ^{22}Si and ^{2}He cluster emission in ^{29}S.

Section 2 focuses on nuclear interactions of weakly-bound systems. A novel transfer reaction method is introduced to extract optical potentials for exotic nuclei, applied systematically to the neutron-halo ^{6}He. Variations in potential depth with energy are exhibited, and the inapplicability of the dispersion relation for ^{6}He + ^{209}Bi is discussed. The notch method and Bayesian approaches developed to constrain potential uncertainties are described.

Section 3 presents complete kinematics measurements for proton-rich nuclei ^{8}B and ^{17}F using the dedicated STARE (Silicon Telescopic Array for Reactions induced by Exotic nuclei) and MITA(Multi-layer Ionization-chamber Telescope Array) detector arrays. The breakup mechanisms—elastic breakup dominating for proton-halo ^{8}B versus inelastic breakup prevailing for ^{17}F—are illustrated, along with the observed sub-barrier fusion enhancement for ^{17}F + ^{58}Ni attributed to continuum couplings.

At the end of each section, discussions and brief summaries are presented, and the final summary of the whole paper as well as outlooks for direct fusion measurements are given in Section 4.

2. Research on Exotic Nuclear Structures and Exotic Decay Modes

As atomic nuclei approach the separation threshold, correlations among a few nucleons within the nucleus become significant, potentially leading to the formation of exotic structures such as halos, skins, and clusters. These structural changes are accompanied by unusual decay modes, including dineutron or diproton correlations and cluster emission.

The nuclear structure of the initial state in nuclear reactions strongly couples with the reaction dynamics. Therefore, it is essential to investigate the exotic structures and unusual decay modes of nuclei near the threshold.

2.1. Halo Structures and Core Enlargement Phenomena in Atomic Nuclei

Since the mid-1980s, halo nuclei have been a research focus in nuclear physics. For neutron halo nuclei, the angular distributions of populated excited states in ^{12}B and ^{12}C were measured via the ^{11}B(d,p) and ^{12}C(d,p) reactions. Using the DWBA and ANC analyses, the density distributions and root-mean-square (rms) radii of valence neutrons in different nuclear states were extracted from the experimental angular distribution data [8,9]. The experimental results confirm that the first excited state of ^{13}C is a single-neutron halo state, marking the first experimental evidence of an excited neutron halo state existing on the β-stability line. Additionally, the second and third excited states of ^{12}B were identified as single-neutron halo states, representing the second example of neutron halo states found near the β-stability line. Due to the Coulomb barrier, proton halos are more difficult to form compared to neutron halos, and thus far, only a few proton halo nuclei have been confirmed. A nuclear reaction team measured the total reaction cross-sections for the secondary radioactive beams of ^{27}P, ^{28}P, and ^{29}S incident on a ^{28}Si target using the transmission method. After incorporating Coulomb and finite-range corrections, the experimental cross-sections were compared with calculations from a modified Glauber model incorporating the optical limit of the eikonal approximation and few-body approaches. The results indicate that ^{27}P and ^{29}S are proton halo nuclei, and a novel phenomenon of core enlargement is observed in ^{27}P and ^{28}P [10].

Building on previous work, a systematic study on the formation of halo nuclei has been conducted. Within the framework of the single-particle potential model, the root-mean-square (rms) radii of various single-particle states were calculated by numerically solving the Schrödinger equation and incorporating experimentally determined binding energies and configuration parameters. By analyzing the relationship between the radii and the separation energies, scaling laws for the valence nucleon distributions in these single-particle states were successfully derived. Based on these scaling laws, we deduced the necessary conditions for the formation of neutron halos and proton halos, and explicitly identified the existence region of proton halos [11,12].

2.2. Research on Two-Proton Correlated Emission Phenomena in Highly Excited States of Nuclei

Highly excited nuclei above the separation threshold represent typical quantum open systems, where their structures and properties undergo systematic evolution, giving rise to new physics characterized by novel structural degrees of freedom and effective interactions. Two-proton emission from highly excited states can provide insights into the configuration and geometry of nucleons within the nucleus, holding significant scientific importance for exploring exotic nuclear structures, nucleon–nucleon correlations, and quantum many-body theories.

The nuclear reaction group has investigated the two-proton emission mechanism and underlying correlations in proton-rich nuclei such as ^{17,18}Ne, ^{28,29}S, and ^{27,28}P [13–16]. The observation of two-proton correlated emission (i.e., ^{2}He cluster emission) from highly excited states of ^{17,18}Ne and ^{28,29}S has been reported. Notably, the case of ^{29}S represents the second observed example of excited-state ^{2}He emission internationally. A comparison among ^{28,29}S and ^{27,28}P suggests that the two-proton halo structure is the primary driver of two-proton correlated emission, rather than the previously assumed highly deformed orbitals. To further investigate the configuration of proton pairs inside the nucleus, an HBT analysis was performed on the momentum correlation functions of two-proton emission

from ^{17,18}Ne. The results indicate that the opening angle between the two protons in ^{17}Ne is approximately 74.5°. This value is in good agreement with theoretical calculations [17], indicating that Bardeen–Cooper Schrieffer/Bose–Einstein condensation-like(BCS/BEC-like) crossover phenomenon may occur in this case, i.e., the surroundings of low density matter [18].

2.3. Study of β-Delayed Decay of Nuclei in the Proton-Rich Drip-Line Region

Nuclei far from the β-stability line possess large decay energies. Following β-decay, they typically populate highly excited states in daughter nuclei, which can subsequently decay through the emission of multiple nucleons or nucleon clusters, as well as fission. These exotic decay modes provide crucial information on the structure of nuclei in the drip-line region and the effective nucleon–nucleon interaction, making them one of the hot topics in international research.

The research team has systematically conducted detailed measurements of the β-delayed decay spectroscopy of proton-rich nuclei in the *sd*-shell [19–23]. A new decay mode of β-delayed two-proton (β2p) emission was discovered in ^{22}Si, enabling the first determination of its mass. Its two-proton separation energy was deduced to be 108 ± 125 keV, indicating that it is a very marginal drip-line nucleus. Significant asymmetries were observed in the β-decays of nuclei such as ^{20}Mg, ^{22}Si, and ^{27}S compared to their mirror nuclei, providing rich experimental data for understanding the isospin-symmetry breaking components in effective nuclear forces. The most complete decay schemes to date for drip-line nuclei, including ^{27}S and ^{26}P, were obtained. The branching ratios for proton and γ decay were determined for the first time, establishing the thermonuclear reaction rates for $^{26}\mathrm{Si}(p,\gamma)^{27}\mathrm{P}$ and $^{25}\mathrm{Al}(p,\gamma)^{26}\mathrm{Si}$. These results provide crucial data for addressing the long-standing problem of the overabundance of ^{26}Al in the Galaxy.

3. Optical Potentials for Weakly Bound Nuclear Systems

The nucleus–nucleus interaction potential is a fundamental physical quantity that must first be determined in the study of nuclear reaction mechanisms. The optical model potential (OMP) is typically used to describe the complex nucleus–nucleus interaction. The term "optical" originates from the physical mechanism in which incident particles undergo scattering or absorption when interacting with the target nucleus, a mechanism similar to how light behaves under analogous conditions. Due to its remarkable effectiveness in accurately predicting elastic scattering and reaction processes, the optical model is regarded as one of the fundamental reaction models in nuclear physics. It is well known that the optical potential is highly sensitive to nuclear structure; therefore, the optical potential for exotic nuclear systems is expected to exhibit characteristics distinct from those of tightly bound systems.

Due to limitations such as the low intensity and poor quality of radioactive ion beams, it is difficult to precisely extract the optical potential for exotic nuclear systems from elastic scattering angular distributions. The nuclear reaction group has proposed an innovative method to extract the optical potential for exotic nuclear systems via transfer reactions [24]. This method offers the following advantages: (1) It allows for the use of existing high-intensity and high-quality stable beams, thereby enabling experiments with relatively high precision, such as in statistics, energy, and angular accuracy. (2) The final states of transfer reactions can be populated to different excited states, which is highly conducive to investigating the energy dependence of potential parameters, and also makes it possible to conduct specialized studies targeting specific nuclear states.

3.1. Optical Potentials for the ^{6}He Halo Nucleus Systems

Over the past decade, ^{6}He has attracted extensive attention from both theoretical and experimental communities due to its two-neutron halo nature and the feasibility of producing intense beams at energies near the Coulomb barrier. The abundant elastic scattering data for the ^{6}He system make it highly suitable for validating the OMP extracted via the transfer reaction method.

Based on this approach, the research team measured the angular distributions of single-proton transfer reactions ^{11}B(^{7}Li,^{6} He)^{12}C, ^{63}Cu(^{7}Li,^{6} He)^{64}Zn, and ^{208}Pb(^{7}Li,^{6} He)^{209}Bi at energies near the Coulomb barrier at the Beijing HI-13 tandem accelerator. The transfer angular distributions were fitted using the DWBA and the coupled reaction channels (CRC) method to extract the optical potential parameters for the outgoing channel of the halo nucleus ^{6}He system.

3.1.1. Optical Potential for the ^{6}He + ^{12}C System

At incident energies of $E_{\mathrm{lab}}(^{7}\mathrm{Li}) = 18.3$ and 28.3 MeV, the angular distributions of the single-proton transfer reaction ^{11}B(^{7}Li,^{6} He)^{12}C were measured [25], as shown in Figure 1. The red curves in Figure 1 represent the DWBA fitting results. The optical potential for the ^{7}Li + ^{11}B incident channel was obtained from previous studies [26]. By fixing the reduced radius $r_0 = 1.25$ fm and diffuseness $a = 0.65$ fm, the proton separation energies were recalculated, and the depths of the potentials for the bound states ^{7}Li = p + ^{6}He and ^{12}C = p + ^{11}B were derived accordingly. The spectroscopic factors for the ground-state protons in ^{7}Li and ^{12}C are 0.89 and 2.85, respectively [27,28]. To optimize the fitting of the transfer angular distributions at different incident energies, a comprehensive grid search was performed for the six potential parameters (V, r_{0V}, a_V, W, r_{0W}, a_W). The fitting process was evaluated through chi-square analysis. Notably, the radius parameter of the real part of the potential is smaller than that of the imaginary part, indicating that the absorption process starts at a larger distance, consistent with the inherently loosely bound structure of the projectile.

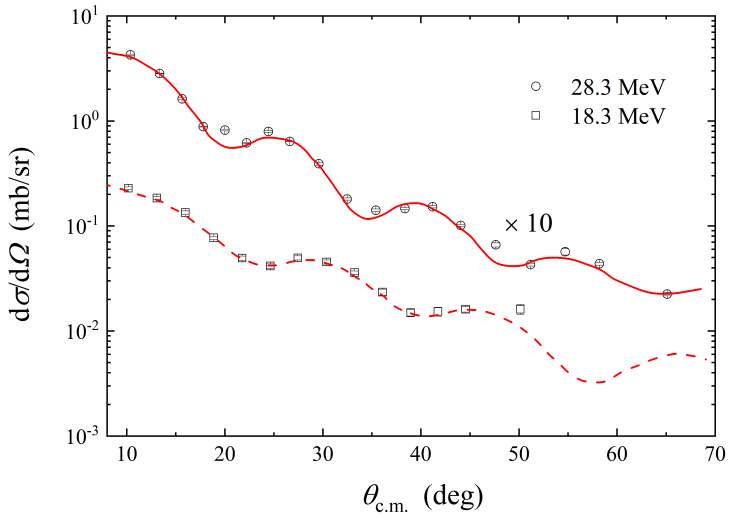


Figure 1. Angular distributions of ^{11}B(^{7}Li,^{6} He)^{12}C at $E_{\mathrm{lab}}(^{7}\mathrm{Li}) = 28.3$ (circles) and 18.3 (squares) MeV, respectively. The solid and dashed curves denote the fitting results with the DWBA approach for the data at 28.3 and 18.3 MeV. Figure is taken from Ref. [25].

3.1.2. Optical Potential for the ^{6}He + ^{64}Zn System

The experiments were performed at laboratory incident ^{7}Li beam energies of 12.67, 15.21, 16.33, 23.30, 27.30, and 30.96 MeV to measure the angular distributions of the transfer reaction ^{63}Cu(^{7}Li,^{6} He)^{64}Zn and the corresponding elastic scattering of ^{7}Li + ^{63}Cu [29]. The optical potential for the incident channel ^{7}Li + ^{63}Cu was obtained by fitting the elastic scattering angular distributions. The angular distributions of the single-proton transfer reaction ^{63}Cu(^{7}Li,^{6} He)^{64}Zn are shown in Figure 2. In the CRC calculations, the coupling effects of the first excited state of ^{7}Li and the first and second excited states of ^{63}Cu were taken into account.

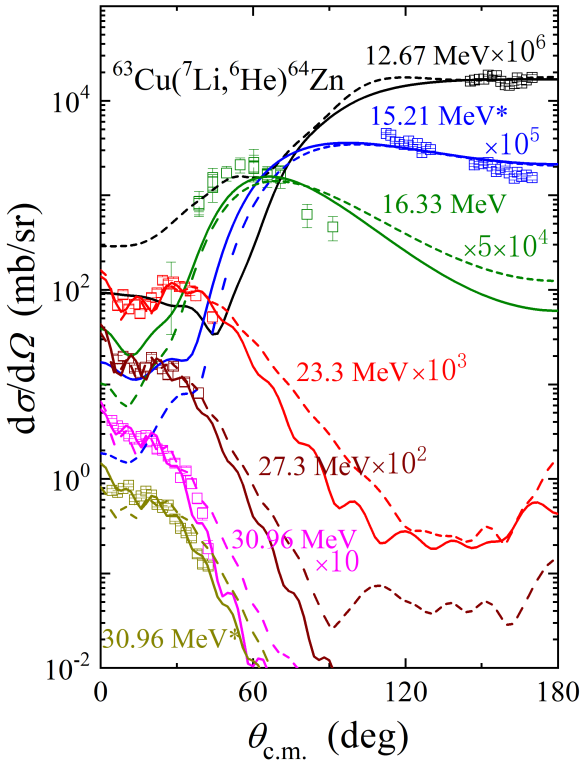


Figure 2. Angular distributions of transfer reactions ^{63}Cu(^{7}Li,^{6} He)^{64}Zn. The squares represent the experimental data, and the solid and dashed curves denote the fitting results with CRC and DWBA approaches, respectively. The figure is taken and modified from Ref. [29].

The energy dependence of the depths of the real and imaginary parts of the optical potential for the ^{6}He + ^{64}Zn system was extracted. The results indicate that, within the studied energy range, the potential parameters obtained from both the DWBA and CRC methods vary around constant values, and there are significant differences between the results from these two methods. Due to the limitation of the ^{7}Li beam energies provided by the HI-13 tandem accelerator, measurements could not be performed in the sub-barrier energy region, and thus the phenomenon of rapid variation of optical potential parameters near the Coulomb barrier was not observed. To verify the reliability of the results, the elastic scattering angular distributions of ^{6}He + ^{64}Zn at $E_{\mathrm{lab}}(^{6}\mathrm{He}) = 10.0$ and 13.6 MeV were recalculated using the obtained potential parameters, with the experimental data taken from Ref. [30], the results are shown in Figure 3.

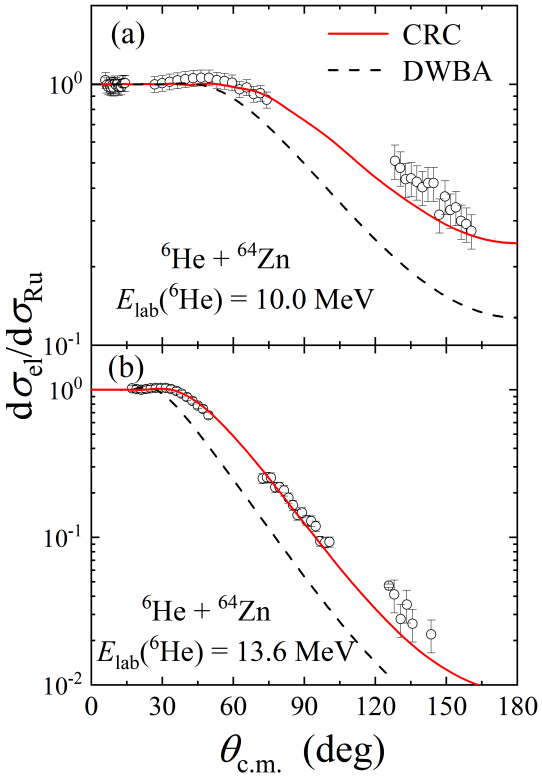


Figure 3. OM calculation results with the OMPs obtained by the CRC (solid curves) and DWBA (dashed curves) approaches and compared with the experimental elastic scattering data of the ^{6}He + ^{64}Zn system at (**a**) E_{lab}(^{6}He) = 10.0 and (**b**) 13.6 MeV. Open circles are the experimental data taken from Ref. [30].

3.1.3. Optical Potential for the ^{6}He + ^{209}Bi System

The angular distributions of the transfer reaction ^{208}Pb(^{7}Li,^{6} He)^{209}Bi were measured near the Coulomb barrier at ^{7}Li laboratory incident energies of 21.20, 24.30, 25.67, 28.55, 32.55, 37.55, and 42.55 MeV. The experimental results are given in Refs. [31–33].

The energy dependence of the real and imaginary potential depths for the ^{6}He + ^{209}Bi system, extracted by the CRC and DWBA methods, is shown in Figure 4. In panel (b), the solid and dashed lines represent piecewise linear fits to the CRC and DWBA results, respectively. The corresponding curves in panel (a) are the real part trends predicted by the dispersion relation based on the fitting results in panel (b).

In the CRC calculations, the coupling effects of the first three excited states of ^{7}Li and the single-neutron transfer channels were taken into account. The results indicate that the potential parameters obtained by the CRC and DWBA methods are essentially the same, suggesting that the coupling channel effects may not be significant for this heavy system. The elastic scattering angular distributions of the ^{6}He + ^{209}Bi system were recalculated using the extracted potential parameters and compared with the existing experimental data [34,35]. The results are shown in Figure 5. It can be seen that the potential parameters obtained by both the CRC and DWBA methods reproduce the experimental data reasonably well, which verifies the reliability of the potential parameters.

To investigate the energy dependence of the potential parameters, linear fits were performed on the imaginary potential depths obtained from the CRC and DWBA methods using piecewise linear functions, with the results shown in Figure 4. It can be observed that, as the system energy decreases, the imaginary potential depth exhibits an increasing trend near the Coulomb barrier, indicating an anomalous threshold anomaly [36].

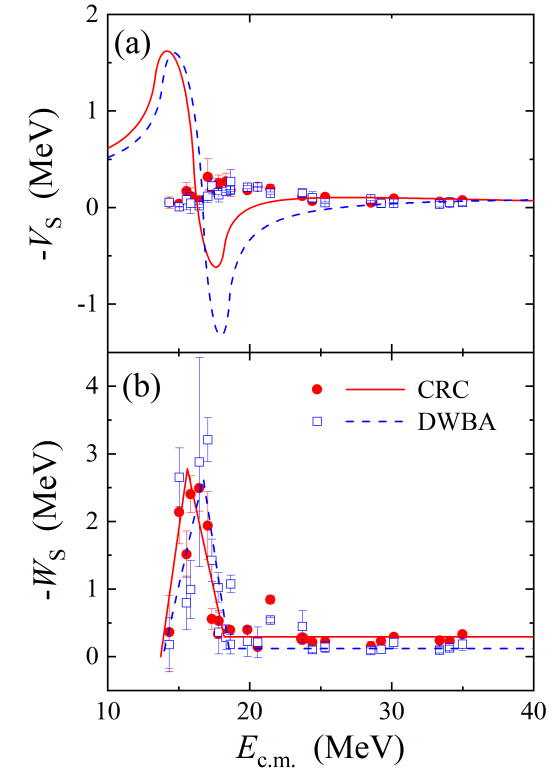


Figure 4. Energy dependence of the real (**a**) and imaginary (**b**) potentials at the sensitive radius of 13.5 fm for the ^{6}He + ^{209}Bi system. The full circles and empty squares denote the CRC and DWBA results from Refs. [31–33]. Solid and dashed curves in (**b**) represent the linear segment fitting for the imaginary potential derived by the CRC and DWBA approaches, respectively. The predictions of the dispersion relation according to the variations of the imaginary potentials are presented in (**a**) by the corresponding curves.

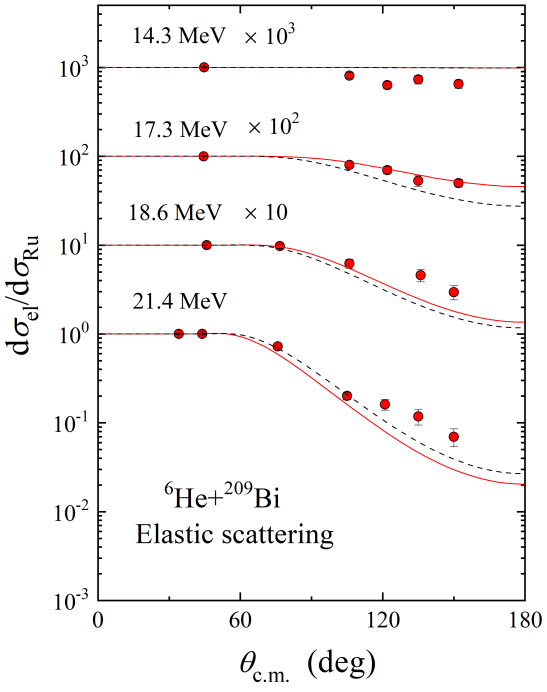


Figure 5. Angular distributions of ^{6}He + ^{209}Bi elastic scattering calculated with OMP parameters extracted from transfers by the CRC (solid curve) and DWBA (dashed curve) approaches, respectively, and compared with the experimental data (circles). The figure is taken from [33].

As the energy further decreases, the imaginary potential depth drops rapidly until it reaches zero. From this, the reaction threshold energy for the ^{6}He + ^{209}Bi system is determined to be $0.68V_B$, marking the first observation of the reaction threshold energy in a halo nucleus system. Compared with the tightly bound system ^{16}O + ^{208}Pb (threshold energy of $0.93V_B$) [37] and the stable weakly bound system ^{6}Li + ^{144}Sm (threshold energy of $0.81V_B$) [38], the lower reaction threshold energy of the ^{6}He + ^{209}Bi system further demonstrates the more diffuse matter distribution of the halo nucleus ^{6}He. Based on the variation trend of the imaginary part, the energy dependence of the real potential depth was calculated using the dispersion relation [39], with the results shown as curves in Figure 4a. The results indicate that the trend of the real depth predicted by the dispersion relation is inconsistent with the experimental findings. The dispersion relation, grounded in causality, is generally regarded as a universal principle widely applied in nuclear physics. These results provide strong evidence that the dispersion relation may not be applicable to exotic nuclear systems. The underlying physical reasons for this discrepancy warrant further in-depth investigation.

3.2. Discussions and Brief Summary

This paper proposes a novel method—the transfer reaction method—which utilizes transfer reactions induced by stable nuclear beams to extract the optical model potential (OMP) for the exit channel of exotic nuclear systems. Using this method, a systematic study of the OMP for ^{6}He halo nucleus systems was conducted. Measurements of the single-proton transfer reactions ^{11}B(^{7}Li,^{6} He)^{12}C, ^{63}Cu(^{7}Li,^{6} He)^{64}Zn, and ^{208}Pb(^{7}Li,^{6} He)^{209}Bi were performed at the Beijing HI-13 tandem accelerator. The transfer angular distributions were fitted using both the CRC and DWBA methods to extract the optical potential parameters for the exit channel halo nucleus systems ^{6}He + ^{12}C, ^{6}He + ^{64}Zn, and ^{6}He + ^{209}Bi.

Based on the energy dependence of the extracted optical potential parameters, an abnormal threshold anomaly in the imaginary potential depth near the Coulomb barrier was clearly observed for the ^{6}He + ^{209}Bi system. Furthermore, a decreasing trend of the imaginary depth with decreasing energy was observed for the first time in the deep sub-barrier energy region, allowing for the extraction of the reaction threshold energy for the ^{6}He + ^{209}Bi system. Concurrently, these results also provide the first evidence that the causality-based dispersion relation is not applicable to this halo nucleus system. The underlying physical reasons for this discrepancy require further investigation.

The method of extracting optical potentials for exotic nuclear systems in the exit channel via transfer reactions offers a novel approach for studying the optical potentials of such systems. The feasibility of this method has been validated in light (^{11}B(^{7}Li,^{6} He)^{12}C), medium-mass (^{63}Cu(^{7}Li,^{6} He)^{64}Zn), and heavy (^{208}Pb(^{7}Li,^{6} He)^{209}Bi) systems. This method can be further extended to other systems to enable in-depth and systematic investigations into the properties of optical potentials for exotic nuclear systems.

4. Study on Reaction Mechanisms of Unstable Proton-Rich Weakly Bound Nuclei

With the improvement of radioactive beam intensity and quality, the capability to deeply investigate the complex interplay between nuclear structure and reaction mechanisms in the energy region near the Coulomb barrier has been enhanced. This energy region serves as a transition zone from classical to quantum regimes, where above-barrier dynamics are governed by classical mechanisms, while below-barrier dynamics are dominated by quantum mechanisms. In this region, coupled-channel effects are particularly significant, resulting in complex reaction mechanisms. The study of reaction mechanisms for weakly

bound nuclei near the Coulomb barrier contributes to a deeper understanding of fundamental quantum issues, such as continuum coupling and coherence-decoherence mechanisms.

For fusion reactions, the presence of breakup reaction channels can have two distinct effects. On the one hand, there is a static effect: the loosely bound structure of weakly bound nuclei lowers the Coulomb barrier of the system, thereby increasing the fusion probability. On the other hand, there is a dynamic effect: breakup of the projectile during the reaction process may reduce the incoming flux of projectile ions, consequently suppressing the fusion probability. In recent years, extensive experimental and theoretical studies have been carried out on weakly bound nuclear systems on the neutron-rich side, and systematic trends of fusion cross-sections for weakly bound nuclei in the neutron-rich region have been preliminarily established [1]: For stable weakly bound nuclei, the total fusion cross-section exhibits normal behavior, while the complete fusion cross-section is suppressed at above-barrier energies. In contrast, for unstable weakly bound nuclei, the total fusion cross-section is characterized by above-barrier suppression and sub-barrier enhancement. Meanwhile, due to the absence of repulsive Coulomb interaction between the valence neutron and the target nucleus, neutron transfer serves as the dominant direct reaction mechanism [30,40,41], demonstrating significant coupling effects on both elastic scattering and fusion reactions [42–44].

However, compared to neutron halo (skin) nuclei (where breakup fragments are neutral neutrons), breakup reactions yielding charged fragments play a more significant role in the fusion process. Unlike weakly bound neutron-rich systems, the Coulomb polarization effect plays a crucial role in proton-rich reaction systems: due to the Coulomb repulsion between the valence proton and the target nucleus, the valence proton is polarized to the side far from the target. Consequently, the core of the projectile acts as a shielding agent, thereby reducing the probability of proton transfer and increasing the breakup probability, which subsequently influences other reaction processes such as elastic scattering and fusion [45–47].

In the proton-rich region, data are scarce and no clear conclusion has been reached. Currently, only a very limited number of experimental results exist, and they are mainly concentrated on two nuclei, ^{8}B and ^{17}F. As a proton halo nucleus, ^{8}B has a proton breakup threshold of only 138 keV. ^{17}F is a proton drip-line nucleus with a proton breakup threshold of 600 keV, and its first excited state is considered to have a proton halo structure. In terms of elastic scattering, the angular distributions of ^{8}B [48–50] and ^{17}F [51–53] with various target nuclei do not show significant suppression of the Coulomb rainbow; meanwhile, Continuum-Discretized Coupled-Channels (CDCC) calculations indicate that the effect of the breakup continuum on elastic scattering is not significant. Regarding breakup reactions, for the ^{8}B system, only inclusive breakup results are currently available, such as ^{8}B + ^{64}Zn [49] and ^{208}Pb [54]; CDCC theoretical calculations suggest that elastic breakup may be the dominant direct reaction mechanism for ^{8}B.

Liang et al. conducted relatively detailed studies on the Coulomb breakup of the ^{17}F + ^{208}Pb system at above-barrier energies [55–57]. By performing both coincidence measurements of breakup fragments ^{16}O and protons, and inclusive measurements, the exclusive (^{16}O-proton coincidence) and inclusive (^{16}O) breakup reaction angular distributions were obtained, respectively. Further theoretical analysis indicates that single-proton stripping is the dominant breakup mechanism. Regarding fusion reactions, current results in the proton-rich region are inconsistent: Aguilera et al. observed a significant enhancement of the fusion cross-section at above-barrier energies for the ^{8}B + ^{58}Ni system [58]; however, the ^{8}B + ^{28}Si [59] and ^{40}Ar [60] systems exhibit suppression of the fusion cross-section at above-barrier energies. For ^{17}F, experimental results on fusion reactions are currently available only for the ^{17}F + ^{208}Pb system [61], whose fusion cross-section trend closely

resembles that of ^{16}O + ^{208}Pb, indicating that the valence proton structure of ^{17}F does not produce a discernible effect on the fusion process.

It is evident that the reaction mechanisms of weakly bound nuclei in the proton-rich region, particularly the influence of breakup channels on fusion reactions and the dynamics of the breakup process itself, remain important issues to be resolved. To address this, we performed complete kinematics measurements for the ^{8}B + ^{120}Sn [62] and ^{17}F + ^{58}Ni [63] systems at the CRIB (Center for Nuclear Study Radioactive Ion Beam Separator) of the University of Tokyo, aiming to gain a deeper understanding of the reaction dynamics of proton drip-line nuclei at near-barrier energies.

4.1. Complete Kinematics Measurement of the ^{8}B + ^{120}Sn System

The experiment was carried out at the CRIB facility. The secondary ^{8}B beam was produced by bombarding a liquid-nitrogen-cooled ^{3}He gas target with a 11.2 MeV/nucleon primary ^{6}Li beam. After purification by CRIB, the intensity of the secondary ^{8}B beam was approximately 10^4 particles per second with a purity of about 20%. The main contaminants were ^{7}Be and ^{3}He. By using an aluminum degrader, ^{8}B beams at two energies around the Coulomb barrier (V_B∼38 MeV) were obtained, namely 38.7 ± 0.5 and 46.1 ± 0.6 MeV (energies at the center of the ^{120}Sn target). The ^{120}Sn target was a self-supporting isotopically enriched foil with a thickness of 2.7 mg/cm^2 and a purity of about 97%. Two parallel plate avalanche counters (PPACs) were placed in front of the target to reconstruct the beam trajectory and determine the reaction position on the target. Reaction products were detected using the STARE (Silicon Telescope Array for Reactions induced by Exotic nuclei) detector array [64]. A schematic view of the array is shown in Figure 6. The array consists of ten silicon telescope units. Each unit comprises three layers of silicon detectors: the first layer is a double-sided silicon strip detector (DSSD) with a thickness of 40–60 μm, providing position and energy information of the reaction products; the subsequent two layers are quadrant silicon detectors (QSD) with thicknesses of 300 and 1500 μm, respectively, used to stop light reaction products. Each detection unit is located approximately 70 mm from the target, resulting in a compact configuration with a large solid angle coverage (∼40% of 4π), enabling high-efficiency coincidence measurements. Based on the ΔE-E two-dimensional spectra and time-of-flight (TOF) information, scattered ^{8}B, as well as reaction products such as ^{7}Be and protons, can be clearly identified [62].

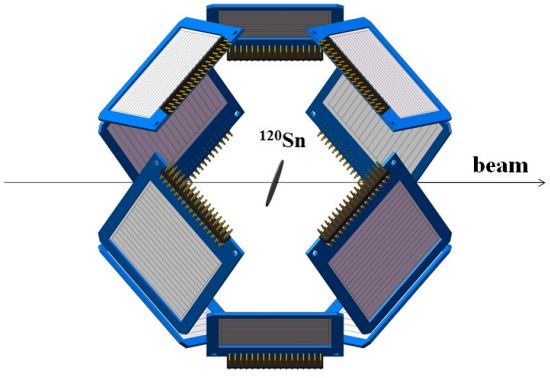


Figure 6. Schematic view of the STARE silicon detector array.

The elastic scattering angular distribution of the ^{8}B + ^{120}Sn system at 38.7 MeV is shown in Figure 7a. The experimental data do not exhibit significant suppression of the Coulomb rainbow. The CDCC calculation results for the elastic scattering angular distribution are shown by the solid curve in the figure, which reproduce the experimental data reasonably well. Details of the CDCC calculations can be found in Ref. [62]. The dashed

curve represents the one-channel calculation results without coupling to continuum states. A comparison reveals that the coupling effects of continuum states lead to a certain suppression of the Coulomb rainbow; however, this effect is not as pronounced as that observed in neutron-halo nuclear systems. The results at 46.1 MeV lead to the same conclusion.

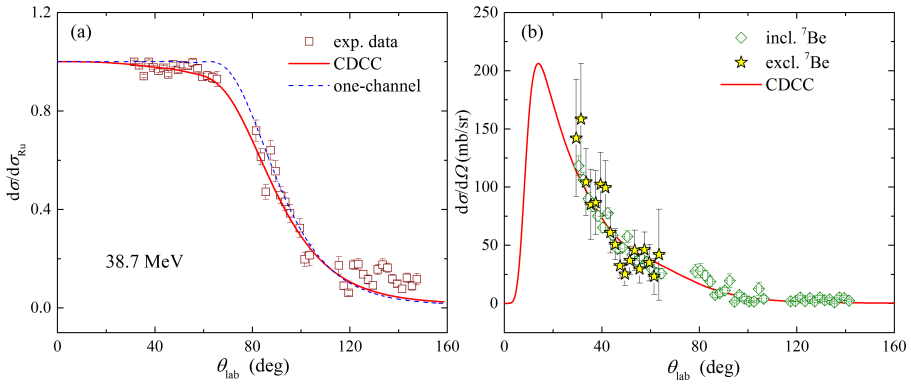


Figure 7. Angular distributions of (**a**) elastic scattering and (**b**) ^{7}Be production for the ^{8}B + ^{120}Sn system at an incident energy of 38.7 MeV. In (**a**), the squares represent the experimental data, while the solid and dashed curves denote the CDCC and one-channel calculation results, respectively. In (**b**), the stars and diamonds correspond to the ^{7}Be angular distributions obtained from coincidence and inclusive measurements, respectively. The solid curves represent the CDCC calculation results. The figure is adapted from Ref. [62].

For the coincidence measurement of the ^{8}B + ^{120}Sn system, the coincidence detection efficiency of the STARE array for breakup fragments must first be determined. In this work, based on the five-dimensional differential cross-section $d\sigma d\Omega_{^{7}\mathrm{Be}} dE_{^{7}\mathrm{Be}} d\Omega_p$ from CDCC calculations, combined with Markov Chain Monte Carlo (MCMC) sampling, the energy $E_{^{7}\mathrm{Be}}$ and angle $\theta_{^{7}\mathrm{Be}}$ of the breakup fragment ^{7}Be, as well as the emission angles θ_p and φ_p of the proton, were sampled from the multi-dimensional parameter space. Assuming the azimuthal angle φ of ^{7}Be emission to be isotropic, the energy E_p of the emitted proton was then obtained from the energy and momentum conservation of the breakup fragments. Thus, the complete kinematic information of the two breakup fragments, ^{7}Be and proton, was derived. By incorporating the geometry of the STARE detector array, the coincidence detection efficiency was determined. The ^{7}Be angular distribution at an incident energy of 38.7 MeV is shown in Figure 7b, where the stars and diamonds represent the experimental results from coincidence and inclusive measurements, respectively. It can be observed that, within the experimental uncertainties, the two sets of data are essentially consistent. This provides the first experimental evidence indicating that the ^{7}Be production mechanism for the proton halo nucleus ^{8}B is dominated by breakup reactions rather than transfer reactions. The CDCC calculation results for the breakup process are also shown in Figure 7b as the solid curve. It is evident that CDCC reproduces the experimental data reasonably well, suggesting that the breakup mechanism for the ^{8}B + ^{120}Sn system is predominantly elastic breakup. The results at 46.1 MeV lead to the same conclusion.

This result is consistent with the measurements for the ^{8}B + ^{64}Zn [49] and ^{208}Pb [54] systems. Although the results for these two systems were obtained from inclusive measurements, the CDCC calculations reproduce the ^{7}Be angular distributions reasonably well. The study indicates that, from light to heavy target regions, the direct reaction mechanism for the proton halo nucleus ^{8}B is predominantly elastic breakup.

The correlation results of the breakup fragments ^{7}Be and proton for the ^{8}B + ^{120}Sn system at an incident energy of 38.7 MeV are shown in Figure 8. Figure 8a presents the relative kinetic energy spectrum reconstructed from the energy correlation of the breakup fragments, which reflects the above-threshold states (resonant or continuum states) through

which ^{8}B undergoes breakup. The solid curve in the figure represents the simulation result based on the five-dimensional CDCC differential cross-section combined with the STARE geometry. It can be seen that the simulation reproduces the experimental data reasonably well, demonstrating the rationality and reliability of the simulation process. Meanwhile, the experimental data exhibit a peak at around 700 keV, which corresponds precisely to the first resonant state of ^{8}B ($E_x = 0.77$ MeV, $J^{\pi} = 1^{+}$, $\Gamma = 35.6$ keV). To investigate the contribution of this resonant state, a simulation was performed based on CDCC calculations for this state, with the result shown as the dashed curve in Figure 8a. It is evident that the contribution of the 1^{+} resonance is small, accounting for only about 4% of the total ^{7}Be yield. Similar conclusions are obtained at the energy of 46.1 MeV. Among the above-threshold states of ^{8}B, only the first resonant state has a relatively long lifetime. Therefore, this result indicates that the breakup of ^{8}B is dominated by a prompt breakup mechanism. The angular correlation of the breakup fragments for the ^{8}B + ^{120}Sn system at 38.7 MeV is shown in Figure 8b. Here, θ_{12} is the opening angle between the two fragments in the laboratory frame, and β is the azimuthal angle of the fragments in the ^{8}B center-of-mass frame. The solid circles represent the experimental data, and the squares denote the simulation results based on the CDCC output. It can be observed that the simulation describes the structure of the experimental data reasonably well.

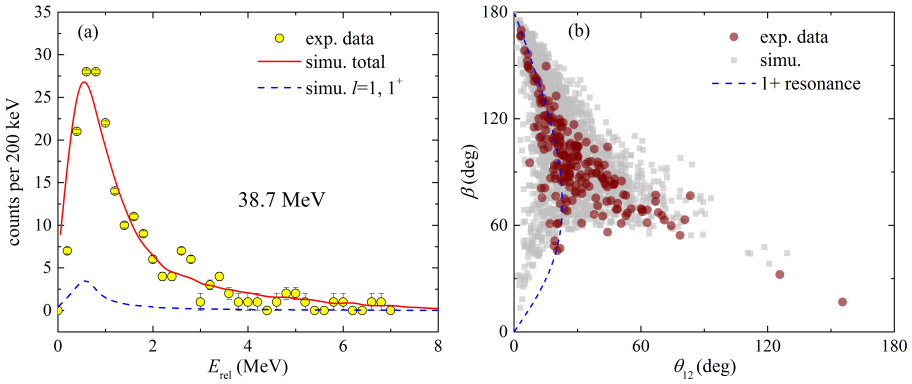


Figure 8. (**a**) Relative energy spectrum and (**b**) angular correlation spectrum for the ^{8}B + ^{120}Sn system at an incident energy of 38.7 MeV. In (**a**), the solid circles represent the experimental data, while the solid and dashed curves denote the simulation results considering l from 0 to 3 and the 1^{+} resonance state with $l = 1$, respectively. In (**b**), the solid circles are the experimental data, and the squares represent the simulation results. The dashed curve corresponds to the simulation result for the 1^{+} resonance state. The figure is adapted from Ref. [62].

The dashed curve represents the theoretical calculation for the first 1^{+} resonant state. It can be observed that most of the experimental data deviate from this curve, once again indicating that the contribution of the 1^{+} resonance is small. On the other hand, θ_{12} is primarily concentrated at small angles, peaking around 30°. From a classical perspective [62], a smaller θ_{12} suggests that the breakup occurs predominantly on the outgoing trajectory, i.e., during the departure from the fusion barrier. Therefore, combining the energy and angular correlations of the breakup fragments leads to the conclusion that the breakup of the proton halo nucleus ^{8}B is dominated by a prompt breakup mechanism on the outgoing trajectory. In this scenario, the breakup process of ^{8}B is not expected to significantly influence complete fusion reactions. For the measurements on the ^{8}B + ^{64}Zn [49] and ^{208}Pb [54] systems, only inclusive measurements were performed, which cannot provide correlation information between the breakup fragments. It is evident that complete kinematics measurements are the only way to gain an in-depth understanding of the reaction mechanisms of unstable nuclei, especially the breakup mechanism.

4.2. Complete Kinematics Measurement of the $^{17}F + ^{58}Ni$ System

The experiment was also carried out at the CRIB facility of the University of Tokyo. A 6.6 MeV/u ^{16}O primary beam was used to produce ^{17}F via bombardment of a D_2 gas target. The thickness of the secondary ^{58}Ni target was 1.0 mg/cm^2. By using aluminum degraders of different thicknesses and varying the pressure of the D_2 gas target, ^{17}F secondary beams at four energies were generated: 43.6 ± 0.7, 47.5 ± 0.7, 55.7 ± 0.8, and 63.1 ± 0.9 MeV. The beam intensity and purity reached 6–10 $\times$ 10^5 particles per second and 85%, respectively. Compared to the ^8B system, the direct reaction product of the ^{17}F system is primarily ^{16}O, which is heavier. Moreover, as the measurements were performed at near- and sub-barrier energies, the products have lower energies. Consequently, low-energy ^{16}O ions may deposit all their energy in the thin silicon detector, making particle identification impossible with a silicon telescope alone. In this scenario, a gas detector must be considered as the first ΔE layer. To address the specific characteristics of the reaction products in the ^{17}F system, the MITA (Multilayer Ionization-chamber Telescope Array) detector array, based on an ionization chamber combined with silicon detectors, was designed [65].

The array consists of 10 independent detection units, with a schematic diagram of each unit shown in Figure 9a. Each unit comprises a front-end ionization chamber (IC) followed by three layers of silicon detectors: the first layer is a double-sided silicon strip detector (DSSD) with a thickness of 40–60 μm, and the subsequent two layers are thick quadrant silicon detectors (QSD) with thicknesses of 300 and 1500 μm, respectively. The detection units are placed symmetrically around the target, with central angles of each unit at $\pm 22.8°$, $\pm 56.4°$, $\pm 90°$, $\pm 123.6°$, and $\pm 157.2°$. The solid angle coverage is close to 8% of 4π. Heavy ions can be identified using the telescope composed of the IC and the DSSD, while light charged particles are identified via the three-layer silicon detector stack. Therefore, based on MITA, simultaneous identification of both heavy and light reaction products for the $^{17}F + ^{58}Ni$ system can be achieved at near-barrier energies [65].

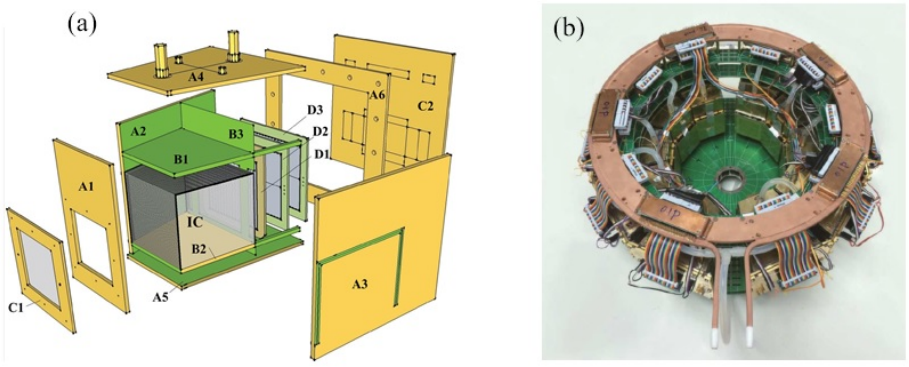


Figure 9. MITA detector array. The MITA array consists of ten independent units. (**a**) Schematic view of a single unit, which includes a front-end ionization chamber (IC) followed by three layers of silicon detectors, labeled D1, D2, and D3, respectively. (**b**) Photograph of the MITA array. Adapted from Ref. [65].

The quasi-elastic scattering angular distributions measured at four energies are shown as open squares in Figure 10. Due to the beam energy spread, events from the inelastic excitation of ^{17}F to its first excited state ($E_x = 0.49$ MeV, $J^\pi = 1/2^+$) could not be resolved experimentally; therefore, the obtained angular distributions are quasi-elastic. Similar to the results for the $^8B + ^{120}Sn$ system, the quasi-elastic angular distributions of $^{17}F + ^{58}Ni$ do not exhibit significant suppression of the Coulomb rainbow. The CDCC and no-coupling (No-CC) calculations are shown by the thin solid and dashed curves in Figure 10, respectively. It can be seen that the difference between them is small, and both reproduce the experimental quasi-elastic angular distributions reasonably well, indicating that the coupling effects of

the breakup continuum on elastic scattering are not significant. The exclusive and inclusive breakup angular distributions are shown as stars and solid circles in Figure 10, respectively. To further understand the breakup process in the ^{17}F reaction, the elastic breakup (EBU) angular distribution was calculated using CDCC, while the non-elastic breakup (NEB) angular distribution was calculated using the IAV model [66]; these are shown as the thick dash-dotted and dashed curves in Figure 10, respectively. The total breakup (TBU) process, being the sum of EBU and NEB, is represented by the thick solid curve in Figure 10, which corresponds to the inclusive breakup results. It is observed that the experimental data from both coincidence and inclusive measurements are well reproduced by the theoretical EBU and TBU calculations. Moreover, within the measured energy range, non-elastic breakup is found to be the dominant breakup process.

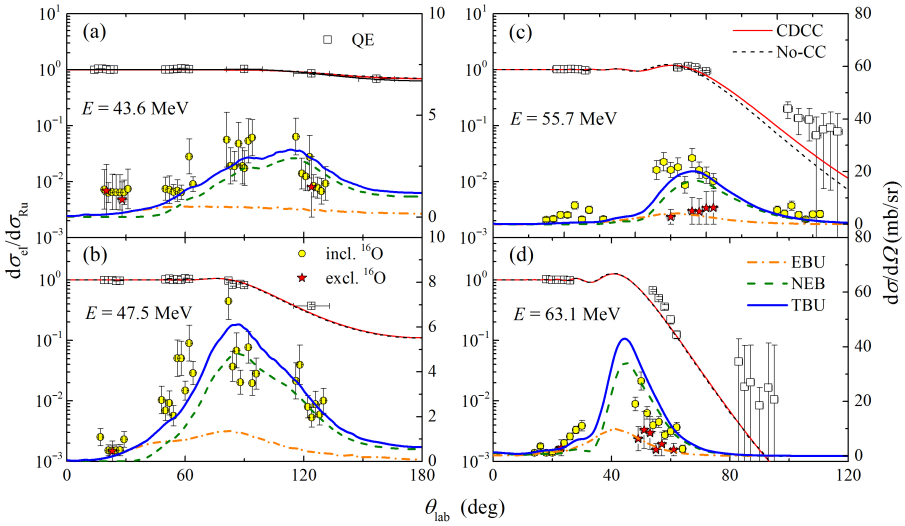


Figure 10. Angular distribution results for the ^{17}F + ^{58}Ni system at (**a**) E_{lab} = 43.6 MeV, (**b**) E_{lab} = 47.5 MeV, (**c**) E_{lab} = 55.7 MeV and (**d**) E_{lab} = 63.1 MeV. The open squares, stars, and solid circles represent the quasi-elastic scattering, exclusive breakup, and inclusive breakup angular distributions, respectively. The thin solid and dashed curves correspond to the CDCC and no-coupling (No-CC) calculation results, respectively, where the coupling to the breakup continuum is omitted. The thick dash-dotted and dashed curves represent the CDCC and IAV model calculations for elastic breakup (EBU) and non-elastic breakup (NEB), respectively. Their sum, representing the total breakup (TBU) process, is shown by the thick solid curve. Adapted from Ref. [63].

On the other hand, the total fusion cross-sections were extracted by measuring fusion evaporation protons and α particles. The results are shown in Figure 11 and compared with the fusion excitation function for the ^{16}O + ^{58}Ni system [67]. To facilitate comparison between different systems, the experimental data were reduced according to the UFF (Universal fusion function) method [68]. As can be seen from the figure, for the above-barrier energy region, the trends of the reduced results for the ^{17}F and ^{16}O reaction systems are essentially consistent. However, in the sub-barrier energy region, the reduced fusion cross-sections for ^{17}F exhibit an enhancement compared to those for ^{16}O. To understand this phenomenon, the total fusion cross-sections for the ^{17}F + ^{58}Ni system were calculated using CDCC. In the calculations, the total fusion cross-sections were obtained by introducing a short-range imaginary potential. This imaginary potential adopts the Woods–Saxon form. For the ^{16}O + ^{58}Ni and p + ^{58}Ni systems, the potential depths are 100 and 50 MeV, the reduced radii are 0.7 and 0.5 fm, and the diffuseness parameter is 0.1 fm, respectively, ensuring that this short-range potential is located inside the Coulomb barrier. The real part of the optical potential for ^{16}O + ^{58}Ni was obtained by reproducing the Coulomb barrier shape of this system [67]; for p + ^{58}Ni, the real potential adopted the KD02 global optical po-

tential [69]. The calculation results indicate that the enhancement of the fusion cross-section for ^{17}F in the sub-barrier region is mainly due to the coupling effects of the continuum states, and this effect becomes increasingly significant as the energy decreases [63]. This conclusion is not entirely consistent with the results for the ^{17}F + ^{208}Pb system [61]. For the ^{17}F + ^{208}Pb and ^{19}F + ^{208}Pb systems, the total fusion cross-sections in the above-barrier region are essentially the same. However, in the sub-barrier region, ^{17}F + ^{208}Pb exhibits a suppression trend in the fusion cross-section compared to ^{19}F + ^{208}Pb [61]. Therefore, the coupling effects of the continuum states in the ^{17}F system with heavy targets require further investigation [63].

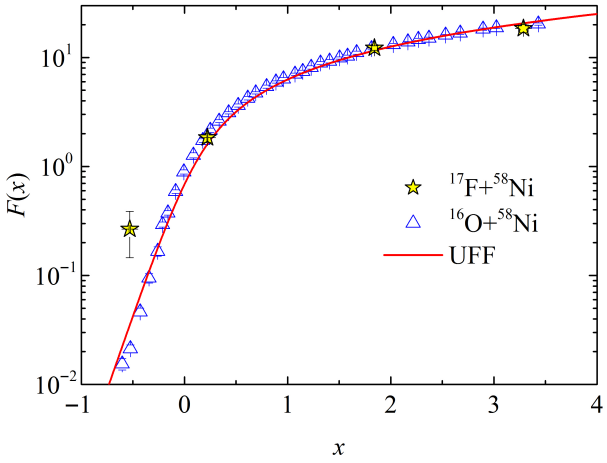


Figure 11. Fusion excitation functions for the ^{17}F + ^{58}Ni and ^{16}O + ^{58}Ni systems. The stars and triangles represent the reduced fusion cross-sections for ^{17}F + ^{58}Ni and ^{16}O + ^{58}Ni, respectively. The solid curve shows the UFF theoretical calculation, serving as a reference standard. Adapted from Ref. [63].

To further investigate the differences in reaction dynamics among unstable weakly bound nuclei, the ratio of the breakup cross-section to the total reaction cross-section for various systems is plotted as a function of the breakup threshold in Figure 12. It can be clearly seen that the breakup probability increases as the breakup threshold decreases. Interestingly, the neutron-rich and proton-rich systems clearly separate into two distinct trends: under the same breakup threshold, proton-rich systems exhibit a lower breakup probability compared to neutron-rich systems. This is primarily due to the additional Coulomb barrier between the valence proton and the core nucleus, which does not exist for valence neutrons. Therefore, unlike neutron halo nuclei, the effective breakup threshold for proton halo nuclei should be the sum of the proton separation energy between the valence proton and the core nucleus and the height of the Coulomb barrier. Currently, experimental data on unstable weakly bound nuclei, especially halo nuclei, are still scarce. To gain a more systematic and comprehensive understanding of the differences between neutron- and proton-halo reaction systems, further studies from both experimental and theoretical perspectives are urgently needed.

4.3. Brief Summary

Complete kinematics measurements for the proton drip-line nuclei ^{8}B + ^{120}Sn and ^{17}F + ^{58}Ni systems were carried out at near-barrier energies at the CRIB facility. Dedicated detector arrays were designed according to the characteristics of the reaction products from different systems to achieve comprehensive identification and high-efficiency measurements. For the proton halo nucleus ^{8}B + ^{120}Sn, coincidence measurements of the breakup fragments ^{7}Be and proton were achieved for the first time, and the complete breakup process was reconstructed through energy and angular correlations. In data analysis, a

Monte Carlo simulation framework based on CDCC was developed, enabling a microscopic description of the breakup process and further revealing the prompt breakup mechanism for the proton halo nucleus ^{8}B in the exit channel. Consequently, the breakup of ^{8}B does not significantly affect the complete fusion process. For the ^{17}F + ^{58}Ni system, information on all reaction channels, including quasi-elastic scattering, breakup, and fusion, was obtained for the first time. The results indicate that the direct reaction mechanism for ^{17}F is dominated by non-elastic breakup processes. Meanwhile, an enhancement of the fusion cross-section was observed for the ^{17}F + ^{58}Ni system in the sub-barrier region. CDCC calculations suggest that this enhancement is mainly due to the coupling effects of the breakup continuum, which become more significant as the energy decreases. Therefore, to clarify the influence of continuum coupling effects on reaction dynamics, further experimental measurements for ^{17}F in the deep sub-barrier region are necessary. Moreover, whether such effects exist for other proton drip-line nuclei, especially proton halo nuclei, warrants further experimental investigation. On the other hand, the differences in reaction mechanisms, particularly the direct reaction dynamics, between ^{8}B and ^{17}F further demonstrate the influence of the proton halo structure on the reaction process. The ground state of ^{8}B possesses a proton halo structure with an extremely low proton separation energy and a very loose configuration, leading to elastic breakup as the dominant direct reaction process. In contrast, the ground state of ^{17}F consists of a ^{16}O core plus a valence proton, with a proton separation energy approximately three times that of ^{8}B. In this structure, the probability of elastic breakup for ^{17}F is reduced, and the direct reactions are dominated by non-elastic breakup processes such as transfer and incomplete fusion. Currently, experimental data on the reaction mechanisms of proton halo nuclei at near-barrier energies remain scarce. Therefore, more related experimental studies are needed to accumulate data and deepen the understanding of the reaction dynamics of proton halo systems.

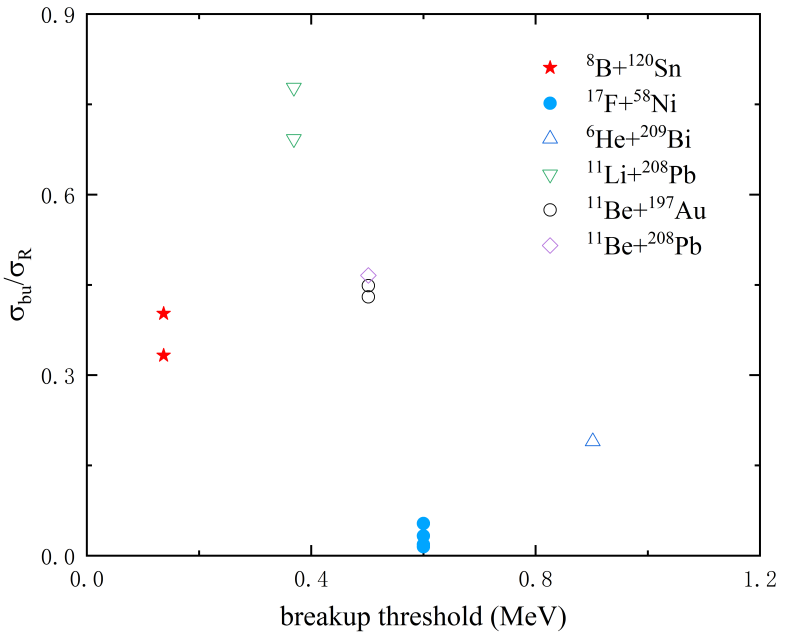


Figure 12. Ratio of the breakup cross-section to the total reaction cross-section as a function of the breakup threshold. Solid symbols represent proton-rich weakly bound nuclei, while open symbols represent neutron-rich weakly bound nuclei. Data for the ^{6}He + ^{209}Bi system are taken from Ref. [34]; for ^{11}Li + ^{208}Pb from Ref. [70]; for ^{11}Be + ^{197}Au from Ref. [71]; and for ^{11}Be + ^{208}Pb from Ref. [72].

5. Summary and Outlook

Over the past decades, our research group has focused on experimental investigations of nuclear interactions and reaction dynamics for exotic nuclear systems at energies around the Coulomb barrier.

Our team has systematically investigated the exotic structures and decay dynamics of nuclei near the particle emission threshold. Using transfer reactions and DWBA/ANC analyses, we confirmed the first excited neutron halo state (^{13}C) on the β-stability line and identified new halo states in ^{12}B. Total reaction cross-section measurements revealed proton halo nuclei ^{27}P and ^{29}S, with a novel core enlargement phenomenon observed in ^{27}P and ^{28}P. Theoretically, we established necessary conditions for halo formation and delineated the existence region for proton halos. Regarding two-proton correlated emission, we observed ^{2}He cluster emission from highly excited states of ^{17,18}Ne and ^{28,29}S, with ^{29}S being only the second such case internationally. In β-delayed decay studies, we discovered a new decay mode, β-delayed two-proton (β2p) emission, in ^{22}Si and determined its mass for the first time. Significant isospin-symmetry breaking was observed in decays of ^{20}Mg, ^{22}Si, and ^{27}S. Complete decay schemes for ^{27}S and ^{26}P provided key nuclear astrophysics data addressing the overabundance of ^{26}Al in the Galaxy. These systematic investigations have significantly deepened our understanding of structural evolution and reaction dynamics in exotic nuclear systems. In our study of nuclear interactions, we systematically investigated the optical model potential for the neutron-halo nucleus ^{6}He using the transfer reaction method. Notably, it was found that the dispersion relation is not applicable in the ^{6}He + ^{209}Bi system, and the underlying physical mechanism remains unclear.

Investigating the reaction mechanisms of exotic nuclear systems at near-barrier energies is the core focus of our work. To deeply analyze the reaction dynamics induced by such weakly bound nuclei, complete kinematics measurements have become the only feasible analytical approach. To this end, we have developed various detector arrays, including the STARE array (for light particles) used in the ^{8}B + ^{120}Sn experiment, and the MITA array (for heavy particles) used in the ^{17}F + ^{58}Ni experiment. The coincidence measurement results for ^{8}B and ^{17}F highlight the critical role of nuclear structure in reaction dynamics. For the proton-halo nucleus ^{8}B, elastic breakup was identified as the dominant direct reaction channel. In contrast, for ^{17}F, which has a valence proton structure and a higher proton separation energy, inelastic breakup becomes the dominant process. A striking observation is that, at a given breakup threshold, the breakup probability of proton-rich nuclei is actually lower than that of neutron-halo nuclei, which may be attributed to the additional Coulomb interaction between the proton and the core/target.

Furthermore, for fusion reactions induced by these unstable nuclei, an enhancement in the total fusion cross-section was observed in the ^{17}F + ^{58}Ni system below the Coulomb barrier. CDCC calculations attribute this enhancement primarily to couplings to the breakup continuum states of ^{17}F. For ^{8}B, despite its higher breakup probability, correlations between breakup fragments suggest that breakup effects do not significantly suppress complete fusion. Currently, fusion cross-sections for unstable nuclei are mainly inferred from fusion–evaporation protons and alpha particles, introducing significant model dependence and uncertainties. Identifying complete and incomplete fusion contributions remains a major challenge. We propose developing a direct measurement technique using an electrostatic or magnetic deflection system at 0° to measure fusion-evaporation residues directly, enabling more reliable cross-section determination. Integrating this system with a high-efficiency detector array for breakup fragments will allow us to obtain correlations between breakup fragments and fusion-evaporation residues. This integrated approach offers a unique opportunity to effectively identify complete and incomplete fusion channels, pro-

viding a promising avenue for comprehensively exploring fusion dynamics, particularly for proton-rich nuclear systems.

Author Contributions: Conceptualization, C.Y., C.L. and L.Y.; investigation, C.Y. and T.L.; resources, F.Y., H.J., N.M. and P.W.; writing—original draft preparation, C.Y. and C.L.; writing—review and editing, C.L. and L.Y.; visualization, C.Y.; supervision, C.L. and L.Y.; project administration, C.L. and L.Y.; funding acquisition, C.L. and L.Y. All authors have read and agreed to the published version of the manuscript.

Funding: This work is supported by the National Key R&D Program of China (Contract Nos. 2022YFA1602302, 2023YFA1606402), the National Natural Science Foundation of China (Grant Nos. 12235020, 12275360, and 12375130) and the Continuous-Support Basic Scientific Research Project.

Data Availability Statement: No new data were created or analyzed in this study. Data sharing is not applicable to this article.

Acknowledgments: All researches were triggered by the halo, thanks to Tanihata-san and his collaborators; more than 100 people were involved in the work, and the authors would like to give thanks to all the participants.

Conflicts of Interest: The authors declare no conflicts of interest.

References

1. Canto, L.F.; Gomes, P.R.S.; Donangelo, R.; Lubian, J.; Hussein, M.S. Recent developments in fusion and direct reactions with weakly bound nuclei. *Phys. Rep.* **2015**, *596*, 1–86. [CrossRef]
2. Tanihata, I.; Savajols, H.; Kanungo, R. Recent experimental progress in nuclear halo structure studies. *Prog. Part. Nucl. Phys.* **2013**, *68*, 215–313. [CrossRef]
3. Pakou, A.; Sgouros, O.; Soukeras, V.; Casal, J.; Rusek, K. Reaction mechanisms of the weakly bound nuclei ^{6,7}Li and ^{7,9}Be on light targets at near barrier energies. *Eur. Phys. J. A* **2022**, *58*, 8. [CrossRef]
4. Yang, L.; Lin, C.J.; Jia, H.M.; Ma, N.R.; Wen, P.W. Experimental investigations on near-barrier reactions with weakly-bound nuclei at the China Institute of Atomic Energy. *Eur. Phys. J. A* **2025**, *61*, 124. [CrossRef]
5. Tanihata, I.; Hamagaki, H.; Hashimoto, O.; Nagamiya, S.; Shida, Y.; Yoshikawa, N.; Yamakawa, O.; Sugimoto, K.; Kobayashi, T.; Greiner, D.E.; et al. Measurements of interaction cross sections and radii of He isotopes. *Phys. Lett. B* **1985**, *160*, 380–384. [CrossRef]
6. Tanihata, I.; Hamagaki, H.; Hashimoto, O.; Shida, Y.; Yoshikawa, N.; Sugimoto, K.; Yamakawa, O.; Kobayashi, T.; Takahashi, N. Measurements of interaction cross sections and nuclear radii in the light p-shell region. *Phys. Rev. Lett.* **1985**, *55*, 2676. [CrossRef]
7. Hansen, P.G.; Jonson, B. The neutron halo of extremely neutron-rich nuclei. *EPL* **1987**, *4*, 409–414. [CrossRef]
8. Liu, Z.H.; Lin, C.J.; Zhang, H.Q.; Li, Z.C.; Zhang, J.S.; Wu, Y.W.; Yang, F.; Ruan, M.; Liu, J.C.; Li, S.Y.; et al. Asymptotic normalization coefficients and neutron halo of the excited states in ^{12}B and ^{13}C. *Phys. Rev. C* **2001**, *64*, 034312. [CrossRef]
9. Lin, C.J.; Zhang, H.Q.; Liu, Z.H.; Wu, W.Y.; Yang, F.; Ruan, M. Nonresonant capture cross sections of ^{11}B(n,γ) and ^{12}C(n,γ) at stellar energies. *Phys. Rev. C* **2003**, *68*, 047601. [CrossRef]
10. Liu, Z.H.; Ruan, M.; Zhao, Y.L.; Zhang, H.Q.; Yang, F.; Ma, Z.Y.; Lin, C.J.; Chen, B.Q.; Wu, Y.W.; Zhan, W.L.; et al. Evidence for enhancement of the total reaction cross sections for ^{27,28}P with a ^{28}Si target and examination of possibly relevant mechanisms. *Phys. Rev. C* **2004**, *69*, 034326. [CrossRef]
11. Lin, C.J.; Zhang, H.Q.; Liu, Z.H.; Wu, Y.W.; Yang, F.; Ruan, M. Scaling laws of valence nucleon distributions for single-particle states. *Phys. Rev. C* **2002**, *66*, 067302. [CrossRef]
12. Liu, Z.H.; Zhang, X.Z.; Zhang, H.Q. Nuclear halo and its scaling laws. *Phys. Rev. C* **2003**, *68*, 024305. [CrossRef]
13. Lin, C.J.; Xu, X.X.; Jia, H.M.; Yang, F.; Jia, F.; Zhang, S.T.; Liu, Z.H.; Zhang, H.Q.; Xu, H.S.; Sun, Z.Y.; et al. Experimental study of two-proton correlated emission from ^{29}S excited states. *Phys. Rev. C* **2009**, *80*, 014310. [CrossRef]
14. Xu, X.X.; Lin, C.J.; Jia, H.M.; Yang, F.; Jia, F.; Wu, Z.D.; Zhang, S.T.; Liu, Z.H.; Zhang, H.Q.; Xu, H.S.; et al. Observation of two-α emission from high-lying excited states of ^{18}Ne by complete-kinematics measurements. *Phys. Rev. C* **2010**, *82*, 064316. [CrossRef]
15. Xu, X.X.; Lin, C.J.; Jia, H.M.; Yang, F.; Jia, F.; Wu, Z.D.; Zhang, S.T.; Liu, Z.H.; Zhang, H.Q.; Xu, H.S.; et al. Investigation of two-proton emission from excited states of the odd-Z nucleus ^{28}P by complete-kinematics measurements. *Phys. Rev. C* **2010**, *81*, 054317. [CrossRef]
16. Xu, X.X.; Lin, C.J.; Jia, H.M.; Yang, F.; Zhang, H.Q.; Liu, Z.H.; Wu, Z.D.; Yang, L.; Bao, P.F.; Sun, L.J.; et al. Correlations of two protons emitted from excited states of ^{28}S and ^{27}P. *Phys. Lett. B* **2013**, *727*, 126–129. [CrossRef]

17. Oishi, T.; Hagino, K.; Sagawa, H. Diproton correlation in the proton-rich Borromean nucleus ^{17}Ne. *Phys. Rev. C* **2010**, *82*, 024315. [CrossRef]
18. Hagino, K.; Sagawa, H.; Carbonell, J.; Schuck, P. Coexistence of BCS- and BEC-like pair structures in halo nuclei. *Phys. Rev. Lett.* **2007**, *99*, 022506. [CrossRef]
19. Xu, X.X.; Lin, C.J.; Sun, L.J.; Wang, J.S.; Lam, Y.H.; Lee, J.; Fang, D.Q.; Li, Z.H.; Smirnova, N.A.; Yuan, C.X.; et al. Observation of β-delayed two-proton emission in the decay of ^{22}Si. *Phys. Lett. B* **2017**, *766*, 312–316. [CrossRef]
20. Sun, L.J.; Xu, X.X.; Fang, D.Q.; Lin, C.J.; Wang, J.S.; Li, Z.H.; Wang, Y.T.; Li, J.; Yang, L.; Ma, N.R.; et al. β-decay study of the $T_z = -2$ proton-rich nucleus ^{20}Mg. *Phys. Rev. C* **2017**, *95*, 014314. [CrossRef]
21. Sun, L.J.; Xu, X.X.; Lin, C.J.; Lee, J.; Hou, S.Q.; Yuan, C.X.; Li, Z.H.; José, J.; He, J.J.; Wang, J.S.; et al. (RIBLL Collaboration) β-decay spectroscopy of ^{27}S. *Phys. Rev. C* **2019**, *99*, 064312. [CrossRef]
22. Liang, P.F.; Sun, L.J.; Lee, J.; Hou, S.Q.; Xu, X.X.; Lin, C.J.; Yuan, C.X.; He, J.J.; Li, Z.H.; Wang, J.S.; et al. Simultaneous measurement of β-delayed proton and γ emission of ^{26}P for the ^{25}Al$(p,\gamma)^{26}$Si reaction rate. *Phys. Rev. C* **2020**, *101*, 024305. [CrossRef]
23. Sun, L.J.; Xu, X.X.; Hou, S.Q.; Lin, C.J.; José, J.; Lee, J.; He, J.J.; Li, Z.H.; Wang, J.S.; Yuan, C.X.; et al. Experimentally well-constrained masses of ^{27}P and ^{27}S: Implications for studies of explosive binary systems. *Phys. Lett. B* **2020**, *802*, 135213. [CrossRef]
24. Lin, C.J.; Yang, F.; Zhou, P.; Zhang, H.Q.; Liu, Z.H.; Ruan, M.; Wu, X.K.; Zhang, C.L. Optical potentials of exotic nuclear systems extracted from transfer reactions. *AIP Conf. Proc.* **2006**, *853*, 81–85. [CrossRef]
25. Wu, Z.D.; Lin, C.J.; Zhang, H.Q.; Liu, Z.H.; Yang, F.; An, G.P.; Zhang, C.L.; Zhang, G.L.; Jia, H.M.; Xu, X.X.; et al. Optical Potential Parameters for Halo Nucleus System ^{6}He + ^{12}C from Transfer Reaction ^{11}B(^{7}Li, ^{6}He)^{12}C. *Chin. Phys. Lett.* **2009**, *26*, 022503.
26. Neuschaefer, G.H.; Stephens, M.N.; Tabor, S.L.; Kemper, K.W. Single proton stripping reactions to ^{12}C. *Phys. Rev. C* **1983**, *28*, 1594. [CrossRef]
27. Cohen, S.; Kurath, D. Spectroscopic factors for the 1p shell. *Nucl. Phys. A* **1967**, *101*, 1–16. [CrossRef]
28. Ring, P.; Werner, E. Distribution of single-particle strengths in the nuclei ^{207}Tl, ^{207}Pb, ^{209}Bi and ^{209}Pb. *Nucl. Phys. A* **1973**, *211*, 198–210. [CrossRef]
29. Yang, L.; Lin, C.J.; Jia, H.M.; Wang, D.X.; Sun, L.J.; Ma, N.R.; Yang, F.; Wu, Z.D.; Xu, X.X.; Zhang, H.Q.; et al. Optical model potentials for ^{6}He + ^{64}Zn from ^{63}Cu(^{7}Li, ^{6}He)^{64}Zn reactions. *Phys. Rev. C* **2017**, *95*, 034616. [CrossRef]
30. Pietro, A.D.; Figuera, P.; Amorini, F.; Angulo, C.; Cardella, G.; Cherubini, S.; Davinson, T.; Leanza, D.; Lu, J.; Mahmud, H. Reactions induced by the halo nucleus ^{6}He at energies around the Coulomb barrier. *Phys. Rev. C* **2004**, *69*, 044613. [CrossRef]
31. Yang, L.; Lin, C.J.; Jia, H.M.; Yang, F.; Wu, Z.D.; Xu, X.X.; Zhang, H.Q.; Liu, Z.H.; Bao, P.F.; Sun, L.J.; et al. Optical model potentials for the ^{6}He + ^{209}Bi reaction from a ^{208}Pb(^{7}Li, ^{6}He)^{209}Bi reaction analysis. *Phys. Rev. C* **2014**, *89*, 044615. [CrossRef]
32. Yang, L.; Lin, C.J.; Jia, H.M.; Wang, D.X.; Ma, N.R.; Sun, L.J.; Yang, F.; Xu, X.X.; Wu, Z.D.; Zhang, H.Q.; et al. Is the dispersion relation applicable for exotic nuclear systems? The abnormal threshold anomaly in the ^{6}He + ^{209}Bi system. *Phys. Rev. Lett.* **2017**, *119*, 042503. [CrossRef]
33. Yang, L.; Lin, C.J.; Jia, H.M.; Wang, D.X.; Ma, N.R.; Sun, L.J.; Yang, F.; Xu, X.X.; Wu, Z.D.; Zhang, H.Q.; et al. Abnormal behavior of the optical potential for the halo nuclear system ^{6}He + ^{209}Bi. *Phys. Rev. C* **2017**, *96*, 044615. [CrossRef]
34. Aguilera, E.F.; Kolata, J.J.; Nunes, F.M.; Becchetti, F.D.; DeYoung, P.A.; Goupell, M.; Guimarães, V.; Hughey, B.; Lee, M.Y.; Lizcano, D.; et al. Transfer and/or Breakup Modes in the ^{6}He + ^{209}Bi Reaction Near and Below the Coulomb Barrier. *Phys. Rev. Lett.* **2000**, *84*, 5058. [CrossRef]
35. Aguilera, E.F.; Kolata, J.J.; Becchetti, F.D.; DeYoung, P.A.; Hinnefeld, J.D.; Horváth, Á.; Lamm, L.O.; Lee, H.-Y.; Lizcano, D.; Martinez-Quiroz, E.; et al. Elastic scattering and transfer in the ^{6}He + ^{209}Bi system below the Coulomb barrier. *Phys. Rev. C* 2001, *63*, 061603(R). [CrossRef]
36. Keeley, N.; Bennett, S.J.; Clarke, N.M.; Fulton, B.R.; Tungate, G.; Drumm, P.V.; Nagarajan, M.A.; Lilley, J.S. Optical model analyses of ^{6,7}Li + ^{208}Pb elastic scattering near the Coulomb barrier. *Nucl. Phys. A* **1994**, *571*, 326–336. [CrossRef]
37. Nagarajan, M.A.; Mahaux, C.C.; Satchler, G.R. Dispersion Relation and the Low-Energy Behavior of the Heavy-Ion Optical Potential. *Phys. Rev. Lett.* **1985**, *54*, 1136. [CrossRef]
38. Figueira, J.M.; Fernández Niello, J.O.; Arazi, A.; Capurro, O.A.; Carnelli, P.; Fimiani, L.; Martí, G.V.; Heimann, D.M.; Negri, A.E.; Pacheco, A.J.; et al. Energy dependence of the optical potential of weakly and tightly bound nuclei as projectiles on a medium-mass target. *Phys. Rev. C* **2010**, *81*, 024613. [CrossRef]
39. Mahaux, C.; Ngô, H.; Satchler, G.R. Causality and the threshold anomaly of the nucleus-nucleus potential. *Nucl. Phys. A* **1986**, *449*, 354–394. [CrossRef]
40. Fernández-García, J.P.; Di Pietro, A.; Figuera, P.; Gómez-Camacho, J.; Lattuada, M.; Lei, J.; Moro, A.M.; Rodríguez-Gallardo, M.; Scuderi, V. Breakup mechanisms in the ^{6}He + ^{64}Zn reaction at near-barrier energies. *Phys. Rev. C* **2019**, *99*, 054605. [CrossRef]
41. Fernández-García, J.P.; Alvarez, M.A.G.; Moro, A.M.; Rodríguez-Gallardo, M. Simultaneous analysis of elastic scattering and transfer/breakup channels for the ^{6}He + ^{208}Pb reaction at energies near the Coulomb barrier. *Phys. Lett. B* **2010**, *693*, 310–315. [CrossRef]

42. Keeley, N.; Alamanos, N.; Kemper, K.W.; Rusek, K. Elastic scattering and reactions of light exotic beams. *Prog. Part. Nucl. Phys.* **2009**, *63*, 396–447. [CrossRef]
43. Raabe, R.; Sida, J.L.; Charvet, J.L.; Alamanos, N.; Angulo, C.; Casandjian, J.M.; Courtin, S.; Drouart, A.; Durand, D.J.C.; Figuera, P.; et al. No enhancement of fusion probability by the neutron halo of ^{6}He. *Nature* **2004**, *431*, 823–826. [CrossRef]
44. Back, B.B.; Esbensen, H.; Jiang, C.L.; Rehm, K.E. Recent developments in heavy-ion fusion reactions. *Rev. Mod. Phys.* **2014**, *86*, 317–355. [CrossRef]
45. Ito, M.; Yabana, K.; Nakatsukasa, T.; Ueda, M. Fusion reaction of halo nuclei: A real-time wave-packet method for three-body tunneling dynamics. *Nucl. Phys. A* **2007**, *787*, 267–274. [CrossRef]
46. Morcelle, V.; Lichtenthäler, R.; Lépine-Szily, A.; Guimarães, V.; Pires, K.C.C.; Lubian, J.; Mendes, D.R., Jr.; de Faria, P.N.; Kolata, J.J.; Becchetti, F.D.; et al. ^{8}B + ^{27}Al scattering at low energies. *Phys. Rev. C* **2017**, *95*, 014615. [CrossRef]
47. Aguilera, E.F.; Amador-Valenzuela, P.; Martinez-Quiroz, E.; Fernández-Arnáiz, J.; Kolata, J.J.; Guimarães, V. Above-barrier fusion enhancement of proton-halo systems. *Phys. Rev. C* **2016**, *93*, 034613. [CrossRef]
48. Aguilera, E.F.; Martinez-Quiroz, E.; Lizcano, D.; Gómez-Camacho, A.; Kolata, J.J.; Lamm, L.O.; Guimarães, V.; Lichtenthäler, R.; Camargo, O.; Becchetti, F.D.; et al. Reaction cross sections for ^{8}B, ^{7}Be, and ^{6}Li + ^{58}Ni near the Coulomb barrier: Proton-halo effects. *Phys. Rev. C* **2009**, *79*, 021601(R). [CrossRef]
49. Spartà, R.; Di Pietro, A.; Figuera, P.; Tengblad, O.; Moro, A.M.; Martel, I.; Fernández-García, J.P.; Lei, J.; Acosta, L.; Borge, M.J.G.; et al. Probing proton halo effects in the ^{8}B + ^{64}Zn collision around the Coulomb barrier. *Phys. Lett. B* **2021**, *820*, 136477. [CrossRef]
50. Mazzocco, M.; Keeley, N.; Boiano, A.; Boiano, C.; La Commara, M.; Manea, C.; Parascandolo, C.; Pierroutsakou, D.; Signorini, C.; Strano, E.; et al. Elastic scattering for the ^{8}B and ^{7}Be + ^{208}Pb systems at near-Coulomb barrier energies. *Phys. Rev. C* **2019**, *100*, 024602. [CrossRef]
51. Zhang, G.L.; Zhang, C.L.; Zhang, H.Q.; Lin, C.J.; Pang, D.Y.; Wu, X.K.; Jia, H.M.; An, G.P.; Wu, Z.D.; Xu, X.X.; et al. Quasi-elastic scattering of the proton drip line nucleus ^{17}F on ^{12}C at 60 MeV. *Eur. Phys. J. A* **2012**, *48*, 65. [CrossRef]
52. Zhang, G.L.; Zhang, G.X.; Lin, C.J.; Lubian, J.; Rangel, J.; Paes, B.; Ferreira, J.L.; Zhang, H.Q.; Qu, W.W.; Jia, H.M.; et al. Angular distribution of elastic scattering induced by ^{17}F on medium-mass target nuclei at energies near the Coulomb barrier. *Phys. Rev. C* **2018**, *97*, 044618. [CrossRef]
53. Rong, C.H.; Rangel, J.; Wu, Y.S.; Zhang, G.L.; Zhang, G.X.; Lin, C.J.; Cardozo, E.N.; Wang, X.Y.; Yang, L.; Ma, N.R.; et al. Study of quasi-elastic scattering of ^{17}F + ^{208}Pb at energies around Coulomb barrier. *Eur. Phys. J. A* **2021**, *57*, 143. [CrossRef]
54. Pakou, A.; Acosta, L.; O'Malley, P.D.; Aguilar, S.; Aguilera, E.F.; Baines, M.; Bardayan, D.; Becchetti, F.D.; Boomershine, C.; Brodeur, M.; et al. Dominance of direct reaction channels at deep sub-barrier energies for weakly bound nuclei on heavy targets: The case ^{8}B + ^{208}Pb. *Phys. Rev. C* **2020**, *102*, 031601(R). [CrossRef]
55. Liang, J.F.; Beene, J.R.; Caraley, A.L.; Esbensen, H.; Galindo-Uribarri, A.; Gross, C.J.; Mueller, P.E.; Schmitt, K.T.; Shapira, D.; Stracener, D.W.; et al. Dynamic polarization in the Coulomb breakup of loosely bound ^{17}F. *Phys. Lett. B* **2009**, *681*, 22–25. [CrossRef]
56. Liang, J.F.; Beene, J.R.; Esbensen, H.; Galindo-Uribarri, A.; Gomez del Campo, J.; Gross, C.J.; Halbert, M.L.; Mueller, P.E.; Shapira, D.; Stracener, D.W.; et al. Elastic scattering and breakup of ^{17}F at 10 MeV/nucleon. *Phys. Rev. C* **2002**, *65*, 051603. [CrossRef]
57. Liang, J.F.; Beene, J.R.; Galindo-Uribarri, A.; Gomez del Campo, J.; Gross, C.J.; Hausladen, P.A.; Mueller, P.E.; Shapira, D.; Stracener, D.W.; Varner, R.L.; et al. Breakup of ^{17}F on ^{208}Pb near the Coulomb barrier. *Phys. Rev. C* **2003**, *67*, 044603. [CrossRef]
58. Aguilera, E.F.; Amador-Valenzuela, P.; Martinez-Quiroz, E.; Lizcano, D.; Rosales, P.; García-Martínez, H.; Gómez-Camacho, A.; Kolata, J.J.; Roberts, A.; Lamm, L.O.; et al. Near-barrier fusion of the ^{8}B + ^{58}Ni proton-halo system. *Phys. Rev. Lett.* **2011**, *107*, 092701. [CrossRef] [PubMed]
59. Pakou, A.; Stiliaris, E.; Pierroutsakou, D.; Alamanos, N.; Boiano, A.; Boiano, C.; Filipescu, D.; Glodariu, T.; Grebosz, J.; Guglielmetti, A.; et al. Fusion cross sections of ^{8}B + ^{28}Si at near-barrier energies. *Phys. Rev. C* **2013**, *87*, 014619. [CrossRef]
60. Zamora, J.C.; Guimaraes, V.; Rogachev, G.V.; Ahn, S.; Lubian, J.; Cardozo, E.N.; Aboud, E.; Assunção, M.; Barbui, M.; Bishop, J.; et al. Direct fusion measurement of the ^{8}B proton-halo nucleus at near-barrier energies. *Phys. Lett. B* **2021**, *816*, 136256. [CrossRef]
61. Rehm, K.E.; Esbensen, H.; Jiang, C.L.; Back, B.B.; Borasi, F.; Harss, B.; Janssens, R.V.F.; Nanal, V.; Nolen, J.; Pardo, R.C.; et al. Fusion cross sections for the proton drip line nucleus ^{17}F at energies below the Coulomb barrier. *Phys. Rev. Lett.* **1998**, *81*, 3341–3344. [CrossRef]
62. Yang, L.; Lin, C.J.; Yamaguchi, H.; Moro, A.M.; Ma, N.R.; Wang, D.X.; Cook, K.J.; Mazzocco, M.; Wen, P.W.; Hayakawa, S.; et al. Breakup of the proton halo nucleus ^{8}B near barrier energies. *Nat. Commun.* **2022**, *13*, 7193. [CrossRef] [PubMed]
63. Yang, L.; Lin, C.J.; Yamaguchi, H.; Lei, J.; Wen, P.W.; Mazzocco, M.; Ma, N.R.; Sun, L.J.; Wang, D.X.; Zhang, G.X.; et al. Insight into the reaction dynamics of proton drip-line nuclear system ^{17}F + ^{58}Ni at near-barrier energies. *Phys. Lett. B* **2021**, *813*, 136045. [CrossRef]
64. Yao, Y.J.; Lin, C.J.; Yang, L.; Ma, N.R.; Wang, D.X.; Zhang, G.L.; Zhang, G.X.; Jia, H.M.; Yang, F. The effects of beam drifts on elastic scattering measured by the large solid-angle covered detector array. *Nucl. Sci. Tech.* **2021**, *32*, 14. [CrossRef]

65. Ma, N.R.; Yang, L.; Lin, C.J.; Yamaguchi, H.; Wang, D.X.; Sun, L.J.; Mazzocco, M.; Jia, H.M.; Hayakawa, S.; Kahl, D.; et al. MITA: A Multilayer Ionization-chamber Telescope Array for low-energy reactions with exotic nuclei. *Eur. Phys. J. A* **2019**, *55*, 87. [CrossRef]
66. Ichimura, M.; Austern, N.; Vincent, C.M. Equivalence of post and prior sum rules for inclusive breakup reactions. *Phys. Rev. C* **1985**, *32*, 431–439. [CrossRef]
67. Keeley, N.; Lilley, J.S.; Wei, J.X.; Dasgupta, M.; Hinde, D.J.; Leigh, J.R.; Mein, J.C.; Morton, C.R.; Timmers, H.; Rowley, N. Fusion excitation function measurements for the ^{16}O + ^{58}Ni and ^{16}O + ^{62}Ni systems. *Nucl. Phys. A* **1998**, *628*, 1–16. [CrossRef]
68. Canto, L.F.; Gomes, P.R.S.; Lubian, J.; Chamon, L.C.; Crema, E. Disentangling static and dynamic effects of low breakup threshold in fusion reactions. *J. Phys. G Nucl. Part. Phys.* **2009**, *36*, 015109. [CrossRef]
69. Koning, A.J.; Delaroche, J.P. Local and global nucleon optical models from 1 keV to 200 MeV. *Nucl. Phys. A* **2003**, *713*, 231–310. [CrossRef]
70. Fernández-García, J.P.; Cubero, M.; Acosta, L.; Alcorta, M.; Alvarez, M.A.G.; Borge, M.J.G.; Buchmann, L.; Diget, C.A.; Falou, H.A.; Fulton, B.; et al. Simultaneous analysis of the elastic scattering and breakup channel for the reaction ^{11}Li + ^{208}Pb at energies near the Coulomb barrier. *Phys. Rev. C* **2015**, *92*, 044608. [CrossRef]
71. Pesudo, V.; Borge, M.J.G.; Moro, A.M.; Lay, J.A.; Nácher, E.; Gómez-Camacho, J.; Tengblad, O.; Acosta, L.; Alcorta, M.; Alvarez, M.A.G.; et al. Scattering of halo nuclei on heavy targets at energies around the Coulomb barrier: The case of ^{11}Be on ^{197}Au. *EPJ Web Conf.* **2017**, *163*, 00045. [CrossRef]
72. Duan, F.F.; Yang, Y.Y.; Lei, J.; Wang, K.; Sun, Z.Y.; Pang, D.Y.; Wang, J.S.; Liu, X.; Xu, S.W.; Ma, J.B.; et al. Elastic scattering and breakup reactions of neutron-rich nucleus ^{11}Be on ^{208}Pb at 210 MeV. *Phys. Rev. C* **2022**, *105*, 034602. [CrossRef]

Disclaimer/Publisher's Note: The statements, opinions and data contained in all publications are solely those of the individual author(s) and contributor(s) and not of MDPI and/or the editor(s). MDPI and/or the editor(s) disclaim responsibility for any injury to people or property resulting from any ideas, methods, instructions or products referred to in the content.